ADVANCED FUNCTIONAL MATERIALS
www.afm-journal.de

Full Color Emission in $ZnGa_2O_4$: Simultaneous Control of the Spherical Morphology, Luminescent, and Electric Properties via Hydrothermal Approach

Yang Zhang, Zhijian Wu, Dongling Geng, Xiaojiao Kang, Mengmeng Shang, Xuejiao Li, Hongzhou Lian, Ziyong Cheng, and Jun Lin**

$ZnGa_2O_4$ and $ZnGa_2O_4$: Mn^{2+}/Eu^{3+} with uniform nanosphere (diameter about 400 nm) morphology have been synthesized via a facile hydrothermal approach. XRD, Raman spectra, XPS, FT-IR, SEM, TEM, photoluminescence (PL), and cathodoluminescecne (CL) spectra are used to characterize the resulting samples. The controlled experiments indicate the dosage of trisodium citrate and pH values are responsible for shape determination of the $ZnGa_2O_4$ products. The possible fast crystallization–dissolution–recrystallization formation mechanism for these nanospheres is presented. Under UV light and low-voltage electron beam excitation, $ZnGa_2O_4$, $ZnGa_2O_4$: Mn^{2+} and $ZnGa_2O_4$: Eu^{3+} emit bright blue, green, and red luminescence, respectively. Based on density functional theory calculations from first principles, the green and red emission are caused by the Mn 3d and Eu 4f electronic structures, respectively. Besides, the dependence of the CL intensity on the calcination temperature and electrical conductivity of the samples is presented. The $ZnGa_2O_4$: Mn^{2+} nanospheres have a higher CL intensity than that of bulk samples under the same excitation condition. The realization of three primary colors from a single host material suggests that full color display based on $ZnGa_2O_4$ nanospheres might be achievable, showing that these materials have potential applications in lighting and display fields.

1. Introduction

Recently, the synthesis of inorganic materials with uniform and specific size and morphology has attracted much attention allowing for their applications in optics, electrics, catalytic, magnetic, and optoelectronics.[1] It is widely accepted that manipulation of the size, shape and dimensionality of nanomaterials is of fundamental and technological importance due to the strong relation between these parameters and their chemical/physical properties.[1e,2] Especially, more and more attention has been paid to luminescent nanomaterials due to the wide range of applications in lighting (e.g., fluorescent tubes and white light-emitting diodes) and display fields (e.g., cathode ray tubes, field emission displays).[3] Among them, WLEDs represent a promising solid-state light approach due to their fascinating merits of energy savings, higher brightness, longer life time and environmental friendliness compared with conventional incandescent and fluorescence lamps.[3f,4] The most common way to obtain white light is to employ the yellow-emitting YAG: Ce^{3+} phosphor and blue InGaN (370–460 nm) chips. Unfortunately, the drawbacks of this method are low color rendering index (CRI < 80) and a high correlated color temperature (CCT) because of the scarcity of red emission. Thus, it is meaningful to develop some novel red-emitting phosphors with improved properties for application in WLEDs.[5] Besides, field emission displays (FEDs) are considered as one promising display techniques due to their potential to provide displays with thin panel, wide viewing, quick response time, high brightness, self emission and a high contrast ratio.[6] Thus, searching for highly efficient phosphors has been a hot topic for material scientists. Compared with CRTs, phosphors used for FEDs must be operated at relatively lower excitation voltages (≤5 kV) and higher current densities (10–100 μA/cm^2), thus, the development of novel phosphors with higher efficiency, superior stability and reasonable conductivity is very meaningful.[7] Moreover, due to the close relation between the resolution and the particle size of the luminescent materials, smaller particle dimensions are prefered to obtain higher resolution. For practical applications, the phosphors with spherical shape are highly needed over other morphologies due to that a) spheres can minimize the light scattering and b) a denser luminescence layer could be developed by high packing densities.[8] Thus, it

Dr. Y. Zhang, Prof. Z. Wu, Dr. D. Geng, Dr. X. Kang, Dr. M. Shang, Dr. X. Li, Dr. H. Lian, Dr. Z. Cheng, Prof. J. Lin
State Key Laboratory of Rare Earth Resource Utilization
Changchun Institute of Applied Chemistry
Chinese Academy of Sciences
Changchun 130022, P. R. China
E-mail: mmshang@ciac.ac.cn; jlin@ciac.ac.cn
Dr. Y. Zhang, Prof. Z. Wu, Dr. D. Geng, Dr. X. Kang, Dr. M. Shang, Dr. X. Li, Dr. H. Lian, Dr. Z. Cheng, Prof. J. Lin
University of the Chinese Academy of Sciences
Beijing 100049, P. R. China

DOI: 10.1002/adfm.201402092

is urgent for us to establish an efficient method to synthesize phosphors with an ideally spherical shape, a narrow size distribution, and highly dispersibility.

Zinc gallate ($ZnGa_2O_4$), an oxide-based normal spinel material, has shown great promise for application in future lighting and display systems due to its superior thermal stability, and good cathodoluminescence (CL) characteristics under electron bombardment in comparison with sulfide phosphors.[9] $ZnGa_2O_4$ exhibits a blue emission due to the wide optical bandgap of about 4.4–4.7 eV, which is attributed to the transition via a self-activation (SA) center of Ga-O groups under excitation by both ultraviolet light and low voltage electrons.[10] In addition, it can also act as an excellent host material for efficient multicolor-emitting materials when doped with transition metal or rare earth ions: $ZnGa_2O_4$: Mn^{2+} for green emission and $ZnGa_2O_4$: Cr^{3+}, $ZnGa_2O_4$: Eu^{3+} for red emission.[11] Nowadays, various synthetic approaches of $ZnGa_2O_4$ have been employed, such as thermal evaporation of ZnO-Ga powders, using Ga_2O_3 or ZnO nanowires as templates, solid state reaction, pulverizing single crystals synthesized by the flux method, sol-gel processing, electrospinning approach, hydrothermal and precipitation methods.[9a,9c,12] It is widely accepted that when the luminescence materials are made into nanoscale, the density of emission sites would be dramatically increased, which is beneficial to improve the luminescence properties.[3e] Besides, computational chemistry approach has aroused fast growing interests as efficient research and development method for exploration of new superior materials due to the success of density functional theory (DFT).[13] While to the best of our knowledge, the synthesis of nanospheres $ZnGa_2O_4$ phosphor with uniform dispersity has not been reported. There are few literatures published on the relation between the electronic structures and the photoluminescence of the $ZnGa_2O_4$ system.[14] Accordingly in this paper, we synthesized $ZnGa_2O_4$ and $ZnGa_2O_4$: Mn^{2+}/Eu^{3+} nanospheres by a facile hydrothermal method with the assistance of organic additive trisodium citrate (Cit^{3-}). The morphological evolution and the growth mechanism for the synthesized $ZnGa_2O_4$ nanospheres have been studied. Furthermore, the influence of Mg^{2+} ions on the crystal electronic structure and luminescence characteristics of $ZnGa_2O_4$: Mn^{2+} samples has been presented. In addition, the electronic properties, chemical bonding and mechanisms of electron transitions in $ZnGa_2O_4$ and Mn^{2+}/Eu^{3+}-doped $ZnGa_2O_4$ systems were studied based on the density functional theory (DFT) calculations from first principles. A systematic study on the photoluminescence (PL) and cathodoluminescence (CL) properties of $ZnGa_2O_4$: Mn^{2+}/Eu^{3+} nanospheres have been carried out in detail. Besides, the relation between the CL intensity with the calcination temperature and electrical conductivity of the samples has been presented. It is found that they are very promising for application in FEDs.

2. Results and Discussion

2.1. Phase Structure and Morphology

The composition and phase purity of the samples were first investigated by XRD. **Figure 1**a–e show the XRD patterns of the as-prepared $ZnGa_2O_4$, those annealed 500 and 1000 °C, Mn^{2+} or Eu^{3+} doped samples as well as the JCPDS card for $ZnGa_2O_4$, respectively. The diffraction peaks of the sample can be indexed as a pure cubic phase $ZnGa_2O_4$, the locations and relative intensity of the diffraction peaks coincide well with the literature values (JCPDS no. 86–0410). It is worth pointing out that the diffraction peaks increase in intensity with the increase of the calcinations temperature due to the increase of crystallinity.[3e] $ZnGa_2O_4$ is a binary compound oxide consisting of ZnO and Ga_2O_3 with the formula AB_2O_4 and has *Fd-3m* space group symmetry ($a = b = c = 8.335$ Å) and crystallizes in the normal spinel structure with the Zn^{2+} ions occupying the tetrahedrally coordinated A sites and the Ga^{3+} ions occupying the octahedrally coordinated B sites, as shown in the crystal structure in Figure 1f.[12b,12c] Their ion radii for the given coordination number (CN) are listed in Table S1. Generally, charge defect is deleterious to the luminescence intensity of phosphors, and it needs enormous energy to destroy the charge balance of the host, such as high temperature and long calcinations time. For six-coordinated ions, the effective compensating factor (φ) of Mn^{2+} ($\varphi = 2.41$) and Mg^{2+} ($\varphi = 2.77$) are much lower than that

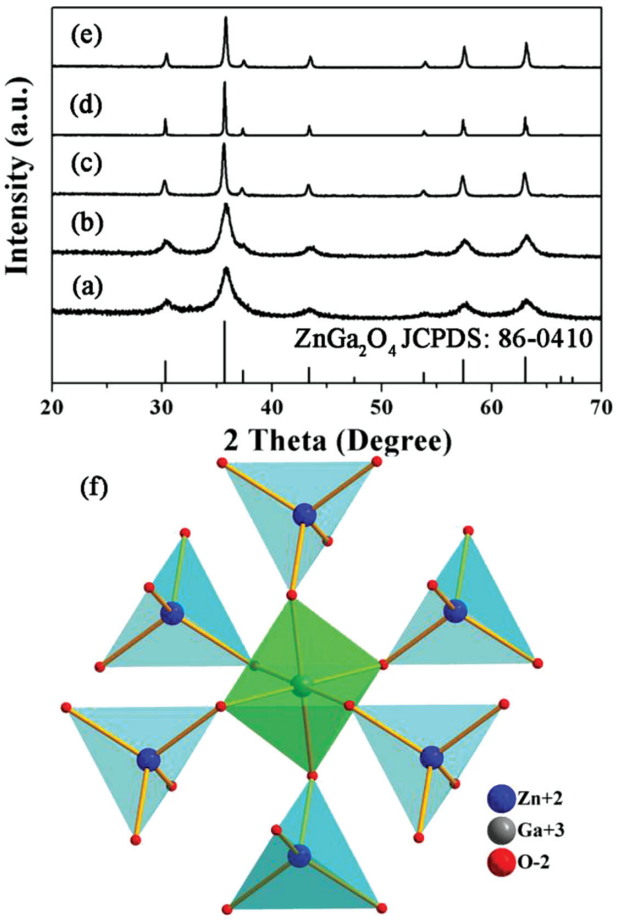

Figure 1. XRD patterns for a) as hydrothermal synthesized samples $ZnGa_2O_4$-HT, the $ZnGa_2O_4$ nanospheres annealed at b) 500 °C, c) 1000 °C, d) $ZnGa_2O_4$: 0.01Mn^{2+}, annealed at 1000 °C, e) $ZnGa_2O_4$: 0.04Eu^{3+}, annealed at 1000 °C. The JCPDS card 86–0410 of $ZnGa_2O_4$ is shown as a reference. f) Crystal structure of $ZnGa_2O_4$ and the coordination environment of Zn and Ga.

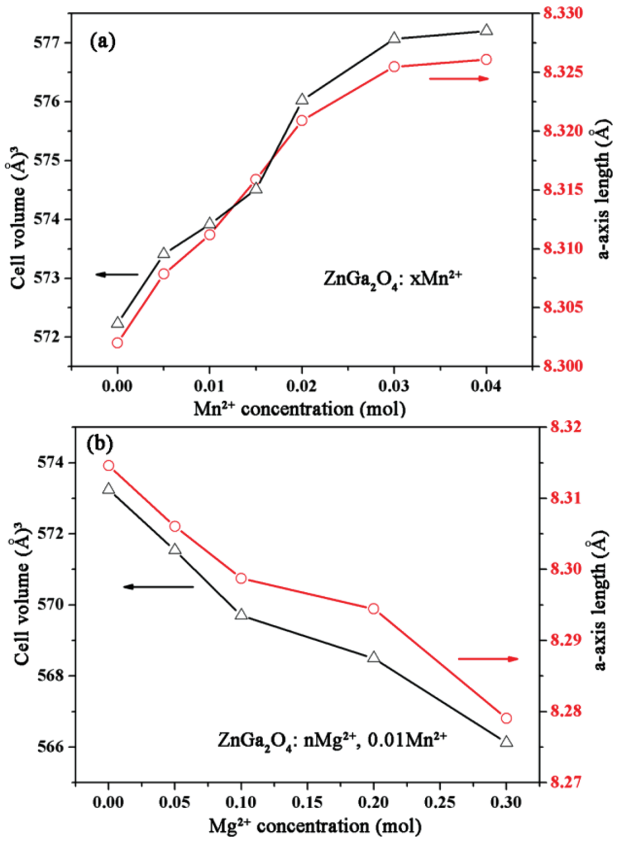

Figure 2. Variation of *a*-axis and cell volume with Mn^{2+} and Mg^{2+} concentrations in $ZnGa_2O_4$: xMn^{2+} and $ZnGa_2O_4$: nMg^{2+}, $0.01Mn^{2+}$ systems, respectively.

of Ga^{3+} ($\varphi = 4.83$), which can be estimated using the following equation $\varphi = Z/r$, where Z is the electric charge number of ion, and r is the ion radius.[3g,3h] Thus, the Mn^{2+} and Mg^{2+} ions would substitute the Zn^{2+} and Eu^{3+} ions would substitute the Ga^{3+} in $ZnGa_2O_4$ considering the similar ion radius and valence, respectively, which could be also confirmed further by the luminescence properties shown in the following paragraphs.[15] The variation of the lattice constants and cell volume with Mn^{2+} and Mg^{2+} ions concentration were calculated from the observed XRD data and are shown in **Figure 2**. Furthermore, the comparison of the Raman spectra of the prepared nanospheres of $ZnGa_2O_4$, $ZnGa_2O_4$: $0.01Mn^{2+}$, $ZnGa_2O_4$: $0.10Mg^{2+}$, $0.01Mn^{2+}$ and $ZnGa_2O_4$: $0.04Eu^{3+}$ indicates that the phonon modes basically don't change at current doping level (Figure S1, Supporting Information). The peaks at 472, 610 and 710 cm^{-1} (or 712 cm^{-1}) can be assigned to the $T_{2g}(2)$, $T_{2g}(1)$ and A_{1g} modes of the cubic spinel-structured $ZnGa_2O_4$, respectively, basically agreeing well with the previous reports.[12a,16]

In order to further examine the chemical composition of the samples, FT–IR spectroscopy was employed for both the hydrothermal prepared sample ($ZnGa_2O_4$-HT) and samples annealed at 1000 °C, as shown in Supporting Information Figure S2a,b. The broad absorption band located at 3425 cm^{-1} can be ascribed to the O–H stretching vibration of water. The COO^- group generated the bands at 1592 cm^{-1} and 1403 cm^{-1}.[17] The two obvious bands at 585 and 465 cm^{-1} can be ascribed to the metal–oxygen (Zn–O and Ga–O) vibrations, respectively.[9a] Although the as-prepared sample was washed several times with water and ethanol, there were still some organic molecules Cit^{3-} on the surface of the particles.[18] When annealed at 1000 °C, the O–H stretching vibration of water and the vibration of COO^- group were barely observed, meanwhile, the metal–oxygen (Zn–O and Ga–O) vibrations (585 and 465 cm^{-1}) were enhanced due to the increase of the crystallinity. The EDX spectra further confirm the presence of C, O, Zn, and Ga elements from the hydrothermal prepared sample (Figure S2c, Supporting Information). After calcination at 1000 °C for 3 h, the element C almost disappears, and the sample mainly consists of O, Zn, and Ga (Figure S2d, Supporting Information), which is consistent with the results of XRD and FT-IR.

The X-ray photoelectron spectrum (XPS) of $ZnGa_2O_4$: $0.01Mn^{2+}$ and $ZnGa_2O_4$: $0.04Eu^{3+}$ nanospheres is displayed in Figure S3 (Supporting Information). The Mn $2p_{1/2}$, $2p_{3/2}$ and Eu $3d_{3/2}$ peaks show binding energies of about 649.4, 639.5 eV and 1146.6 eV, respectively. However, the intensities are much weaker than other elements because of the low doping concentration. The enlarged XPS spectrum of O 1s at 532.2 eV is displayed in Figure S3c (Supporting Information). The fine XPS spectrum reveals Ga 3d at 21.5 eV (Figure S3d, Supporting Information). In addition, the XPS spectrum reveals Ga $2p_{3/2}$ and Ga $2p_{1/2}$ peaks at 1118.5 eV and 1145.9 eV with energy difference about 27.4 eV (Figure S3a,b, Supporting Information), which agrees well with the previous report.[12a] As displayed in Figure S3e (Supporting Information), the enlarged XPS spectrum shows Zn $2p_{3/2}$ and Zn $2p_{1/2}$ peaks at 1021.4 eV and 1044.6 eV with band gap about 23.2 eV, which is nearly the same as the reference.[12a] The C 1s presents peak at about 284.6 eV, which may come from the hydrothermal synthesis process.

Typical SEM, TEM and HRTEM images of the $ZnGa_2O_4$ nanospheres prepared at pH = 5 with $M:Cit^{3-}$ = 1:2 are displayed in **Figure 3**. It should be mentioned that doping a small amount (<5 mol%) of other metal ions (Mn^{2+} and Eu^{3+}) in the

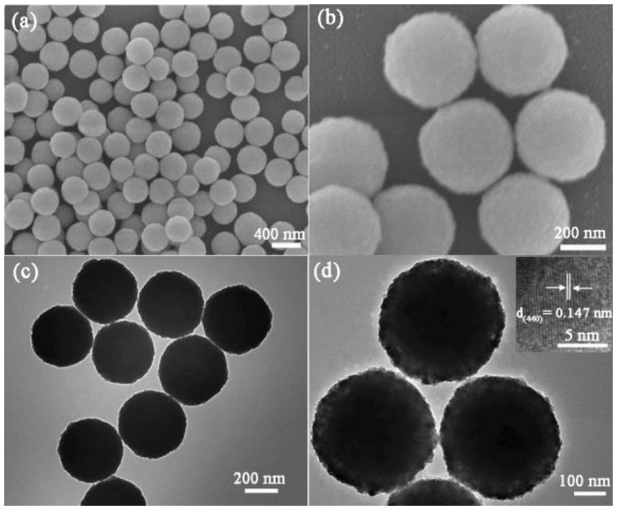

Figure 3. a) Low and high b) magnification SEM images of the $ZnGa_2O_4$ samples prepared at pH = 5 with M/Cit^{3-} = 1:2. c) TEM and d) HRTEM images of the $ZnGa_2O_4$-HT samples.

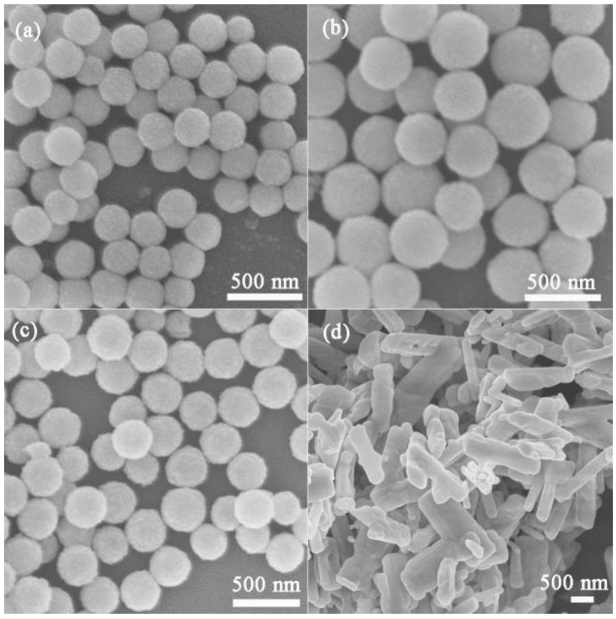

Figure 4. SEM images of $ZnGa_2O_4$-HT nanospheres with different post calcinations temperatures: a) 500 °C, b) 700 °C, c) 1000 °C, and d) $ZnGa_2O_4$-SSR, 1200 °C.

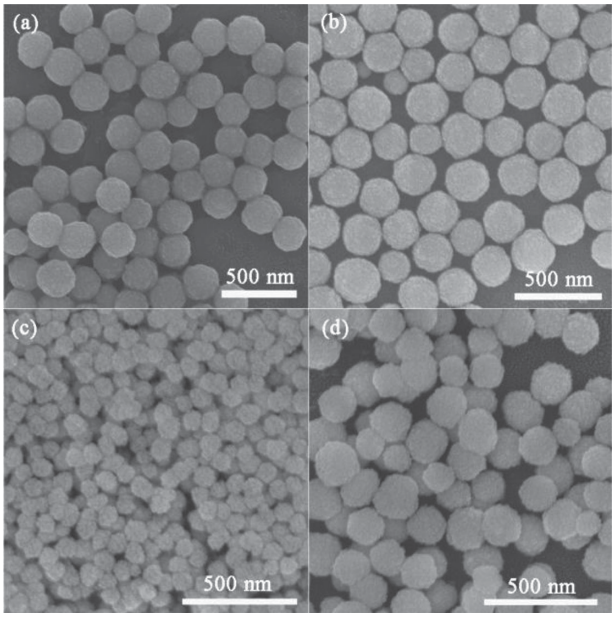

Figure 5. SEM images of the $ZnGa_2O_4$: $n$$Mg^{2+}$, 0.01$Mn^{2+}$ samples doped with different amount of Mg^{2+}: a) n = 0.05, b) n = 0.10, c) n = 0.20, and d) n = 0.30.

$ZnGa_2O_4$ host does not change the phase, crystallization, and morphology of the $ZnGa_2O_4$ products in our present work. So here we only take $ZnGa_2O_4$ as a typical example to explain the morphology of the products. From the low and high-magnification SEM images in Figure 3a,b, we can clearly see that high yield, monodisperse and hierarchical nanospheres with diameter about 400 nm can be prepared by this approach. The peripheral surface of the hierarchical nanosphere is not smooth and contains many nanoparticles with diameters of about 20 nm. The TEM images (Figure 3c) also confirm the morphology of the nanospheres in the samples, corresponding well with the above SEM results. It is obvious that these nanospheres consist of subunits of smaller crystalline primary grains. However, these nanospheres are highly uniform and homogeneously dispersed, which is beneficial to improve the luminescence property. In the HRTEM image (Figure 3d), the obvious lattice fringes confirm the high crystallinity of the samples. The adjacent lattice fringes can be calculated to 0.147 nm, which can be well indexed as d-spacing value of the (440) plane of $ZnGa_2O_4$. Moreover, in order to compare with the morphology of $ZnGa_2O_4$-SSR, the $ZnGa_2O_4$-HT samples were subjected to further heat treatment at different temperatures (500, 700, and 1000 °C). It can be seen that these nanospheres still keep the original morphologies although experiencing the annealing process even annealed up to 1000 °C (**Figure 4**a–c) except for a little size shrunk. However, the $ZnGa_2O_4$-SSR sample is composed of uneven microrods as shown in Figure 4d.

As for $ZnGa_2O_4$: $n$$Mg^{2+}$, 0.01$Mn^{2+}$ samples, the low doping concentration of Mg^{2+} ions did not change the morphology of the $ZnGa_2O_4$: 0.01Mn^{2+} samples (n = 0.05 and 0.10), as shown in **Figure 5**a,b. However, the surface of the nanospheres becomes rougher and the diameter decreases in the obtained products with increased Mg^{2+} ions substitution concentration. Especially with the Mg^{2+} concentration increased up to 0.20 and 0.30, the phase segregation begins to appear and thus the morphology of products changes to some extent (Figure 5c,d).[7b]

Generally, successful synthesis of nano/micro-materials in a solution-based system not only depends on the intrinsic structure of the target compounds but also requires more fastidious control of the growth parameters such as temperatures, organic additives, pH values and so forth.[18,19] The controlled experiments indicate that the addition of trisodium citrate (Cit^{3-}) and pH values play a critical role in determining the crystal structure and morphologies of the final $ZnGa_2O_4$. Without Cit^{3-}, the product is mainly composed of microrods with length about 5 μm and diameter about 0.5–1 μm, as shown in **Figure 6**a. However, the XRD patterns of this sample can be indexed as a pure orthorhombic phase GaOOH (JCPDS no. 54–0910), which is different with the XRD patterns of the samples with adding Cit^{3-} as shown in Figure S4 (Supporting Information). Note that the crystalline phases of the as-prepared products remain unchanged, however, the corresponding morphologies (Figure 6b–6d) have a drastic change relative to those obtained in the presence of different among of Cit^{3-}. From the SEM images shown in Figure 6b, it can be seen clearly that the product is mainly composed of nanospheres with diameter about 300 nm and nanorod bundles with length about 1 μm and diameter about 200 nm, when M:Cit^{3-} = 1:1. With the increase of the amount of Cit^{3-} (M:Cit^{3-} = 1:4), the nanorod bundles disappeared and the product is mainly composed of nanospheres (Figure 6c) with diameter about 400 nm. Figure 6d presents that the sample is seriously aggregated due to the high dosage of Cit^{3-} (M:Cit^{3-} = 1:6). From the crystal structure and morphological evolutions discussed above, we

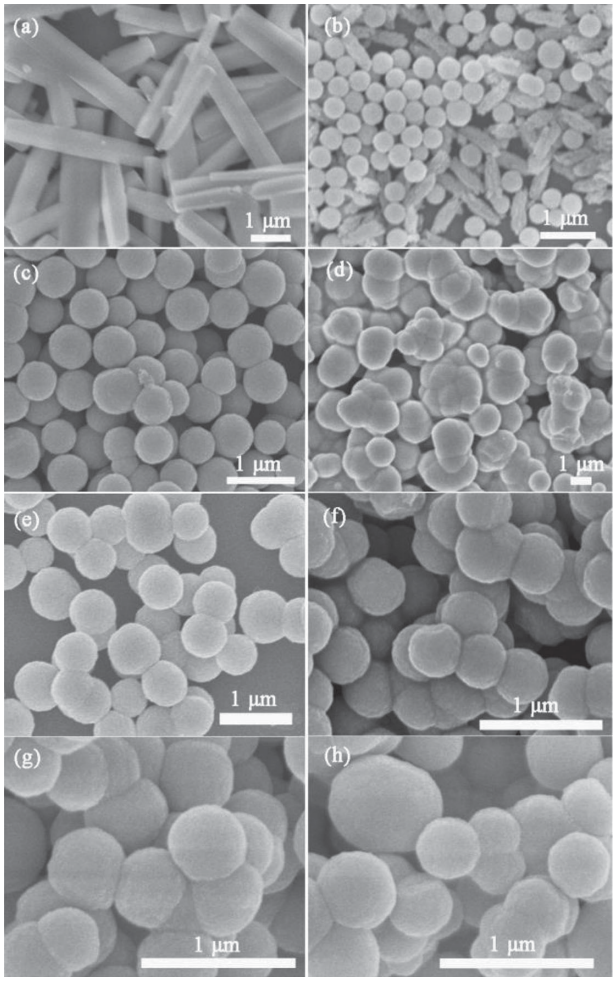

Figure 6. The SEM images of products prepared at 180 °C for 12 h with different dosage of Cit^{3-} and pH values: a) without Cit^{3-}, b) M:Cit^{3-} = 1:1, c) M:Cit^{3-} = 1:4, and d) M:Cit^{3-} = 1:6, with pH = 5; e) pH = 6, f) pH = 7, g) pH = 8 , and h) pH = 9, with M:Cit^{3-} = 1:2.

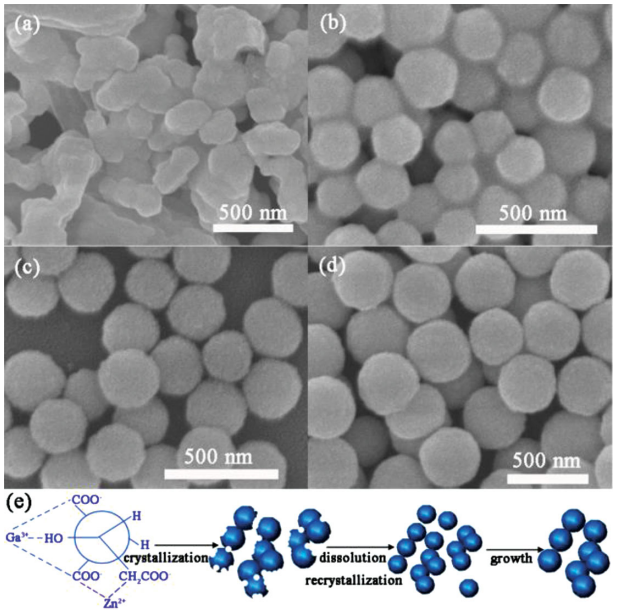

Figure 7. SEM images of as-prepared $ZnGa_2O_4$ sample for different reaction time: a) 1 h, b) 3 h, c) 6 h, and d) 9 h with M:Cit^{3-} = 1:2, pH = 5. e) Schematic illustration for the formation process of $ZnGa_2O_4$ hierarchical nanospheres.

can conclude that organic additive Cit^{3-} has an important influence on the final $ZnGa_2O_4$ products in our current synthesis. Figure 6e–h show the SEM images of $ZnGa_2O_4$ prepared at 180 °C for 12 h with M:Cit^{3-} = 1:2 at pH values of 6, 7, 8, and 9, respectively. It can be seen clearly that all the samples composed of nanospheres, however, the dispersity of the samples becomes worse with the increase of pH from 5 to 9, which may be due to the fast hydrolysis of Zn^{2+} and Ga^{3+} at high pH values.[12d] In addition, the ability of Cit^{3-} being adsorbed to certain crystal facets is different from each other under different pH conditions.[20] Thus, choosing an optimal condition (M:Cit^{3-} = 1:2, pH = 5) is predominant to synthesize $ZnGa_2O_4$ with an ideally spherical shape, a narrow size distribution, and non-agglomeration.

In order to further understand the formation and evolution of $ZnGa_2O_4$ nanospheres, time-dependent experiments on the morphologies of the products were conducted. **Figure 7** shows the SEM images of $ZnGa_2O_4$ nanospheres (M:Cit^{3-} = 1:2, pH = 5) prepared at 180 °C with different reaction times. In a solution-phase synthesis, through the interaction between capping agents with the metal ions, organic additives can change the order of the free energies of different facets, thus affect the relative growth rates of different facets and result in different morphologies.[18,19,21] In our system, Cit^{3-} reacts with Zn^{2+} and Ga^{3+} to form Zn^{2+}-Cit^{3-}-Ga^{3+} complexes in the beginning. In view of the dynamic process, the concentration of free Zn^{2+} and Ga^{3+} ions would be restricted by the formation of such complexes and thus help to control the nucleation and growth of the crystals.[22] Then, Cit^{3-} as a structure-directing reagent could absorb to the surface of crystals, influencing the growth rate of different facets of the crystal, resulting in the formation of the nanospheres.[23] For the sample prepared at a reaction time of 1 h (Figure 7a), nanoparticles with broad size distribution and irregular morphology are formed because of the fast crystallization. With the proceeding of the hydrothermal conditions (high temperature and pressure), the firstly formed nuclei would dissolve and release Zn^{2+} and Ga^{3+} ions gradually. This process can slow down the nucleation and subsequent crystal growth of the $ZnGa_2O_4$ particles.[24] As shown in Figure 7b, the irregular nanoparticles disappeared, while nanospheres became the exclusive products, which is beneficial to decrease the free energy of the system.[21b,23] With the reaction further proceeding for 6 and 9 h, the spherical morphology was preserved and the size of the spheres further increased (Figure 7c,d). The experiment results indicate that the surface of the spheres becomes coarser and the size of nanospheres increases with the increase of reaction time, which may be caused by the increase of the crystallinity. On the basis of the above discussion, it has been suggested that the formation of $ZnGa_2O_4$ nanospheres may result from a fast crystallization–dissolution–recrystallization growth mechanism, which is schematically illustrated in Figure 7e.

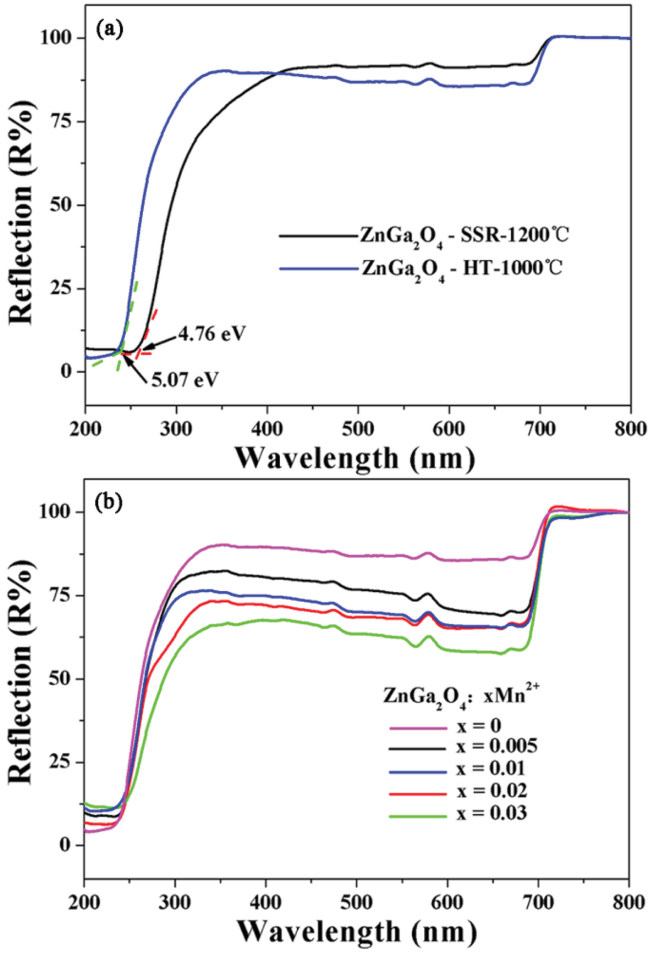

Figure 8. Reflection spectra of the a) $ZnGa_2O_4$ host synthesized by the hydrothermal method and solid state reaction and b) $ZnGa_2O_4$: xMn^{2+} samples.

2.2. Luminescence Properties and Density Functional Theory (DFT) Calculations

2.2.1. PL Properties

As a kind of self-activated phosphor, $ZnGa_2O_4$ exhibits blue emission, with a wide optical band gap of about 4.4–4.7 eV, thus, and its luminescence properties were also studied.[10] **Figure 8**a shows the diffuse reflection spectra of the $ZnGa_2O_4$ synthesized by hydrothermal method and solid state reaction, respectively. The $ZnGa_2O_4$-HT-1000 °C host material shows energy absorption in the 200–300 nm region and the band gap was estimated to be about 5.07 eV, which is larger than the result of the solid state method (about 4.76 eV). The blue shift (about 0.31 eV) in the optical band should result from the quantum size effect and shortening of the Ga-O bond length in the nanoscale of $ZnGa_2O_4$, which is consistent with previous report.[9b] **Figure 9**a shows the excitation and emission spectra of undoped $ZnGa_2O_4$ nanospheres. The excitation spectrum monitored at 365 nm shows a broad band from 225 to 275 nm with a maximum at 245 nm. Upon excitation with 245 nm UV, the emission spectrum of the $ZnGa_2O_4$ sample consists of a broad band ranging from 300 to 500 nm with the peak position at 365 nm, which can be attributed to the self-activation center of the octahedral Ga-O group in the spinel lattices.[9c,12b]

Intentional introduction of impurities (activators) into inorganic phosphors is fundamental to control their optical properties.[10,25] This has worked very well for $ZnGa_2O_4$ powders: undoped $ZnGa_2O_4$ powder is a blue-emitting phosphor, while the Mn^{2+} activated $ZnGa_2O_4$ powders emit bright green luminescence, as shown in Figure 9b. The excitation spectrum monitored at 506 nm includes two broad bands: a very strong band from 200 to 250 nm with a maximum at 234 nm and a weak broad band from 250 to 350 nm with a maximum at 286 nm, which can be ascribed to the absorption of the host $ZnGa_2O_4$, in particular, the Ga-O group, and the charge-transfer transition of Mn^{2+} ions, respectively.[9a] In addition, as displayed in Figure 8b, the absorption intensity of the band about 250–350 nm increases with increasing Mn^{2+} concentration comparing with the host absorption, which provides further confirmation of the absorption originating from Mn^{2+} ions. Furthermore, the enlarged photoluminescence excitation spectrum (350–450 nm) shows five bands centered at 363, 383, 415, 427, and 450 nm corresponding to the well known transitions of Mn^{2+} ion $^5A_1$–^4E, $^6A_1$–$^4T_2$, $^6A_1$–$^4A_1$, $^4E_1$ and $^6A_1$–^4T, respectively, as shown in Figure S5. Under the excitation of 234 nm UV light, the nanospheres of $ZnGa_2O_4$: $0.01Mn^{2+}$ exhibit a green emission band with a peak at 506 nm (Figure 9b, black line), which is attributed to the Mn^{2+} $^4T_1$–$^6A_1$ d-electronic states spin-forbidden transition.[7b,26] This indicates an efficient energy transfer from $ZnGa_2O_4$ host lattice to the doped Mn^{2+} ions, which is consistent with previous reports.[9a,10] As we know, the transitions of Mn^{2+} $^4T_1$–$^6A_1$ within the 3d shell are strongly coupled to lattice vibration and affected by crystal field strength and site symmetry. If Mn^{2+} ions lie in the weak crystal field condition (tetrahedral surrounding), the splitting of the excited d energy levels will be small, resulting in Mn^{2+} emission with higher energy, which results in green emission; if in strong crystal field condition (octahedral surrounding), a yellow/red emission is usually obtained.[7b,27] As mentioned earlier, Mn^{2+} ions substitute for the tetrahedrally coordinated Zn^{2+} ions in the cubic $ZnGa_2O_4$ host, thus, Mn^{2+} gives green emission, which is consistent with the spectral result. When Mg^{2+} is co-doped into $ZnGa_2O_4$: Mn^{2+}, the emission intensity would vary due to the change of the effective crystal field of tetrahedrally coordinated Mn^{2+} ions. Codoping Mg^{2+} ions into the host would create excited state which is consist of 3s and 3p energy levels near the lowest unoccupied molecular orbitals of Mn^{2+} ions. Compared with the $3d^5$ transition of Mn^{2+}, the transition from the Mg^{2+} levels to ground state of Mn^{2+} becomes more easily due to the more spin allowed property. Thus, the auxiliary transition from Mg^{2+} to Mn^{2+} would play a critical role in the enhancement of luminescence intensity of Mg^{2+} ions codoped $ZnGa_2O_4$: $0.10Mg^{2+}$, $0.01Mn^{2+}$ samples as shown in Figure 9b (green line), considering the fact that the probability of $3d^5$ transition of Mn^{2+} itself is very low.[7b,28] As shown in **Figure 10**, it is obvious that the optimum doping concentration of of Mn^{2+} ions is $x = 0.01$, and then decreases sharply with further increasing its concentration due to the concentration quenching effect.[5,29] As for $ZnGa_2O_4$: xMn^{2+}, a rough estimation of the critical distance R_C between Mn^{2+} ions can be

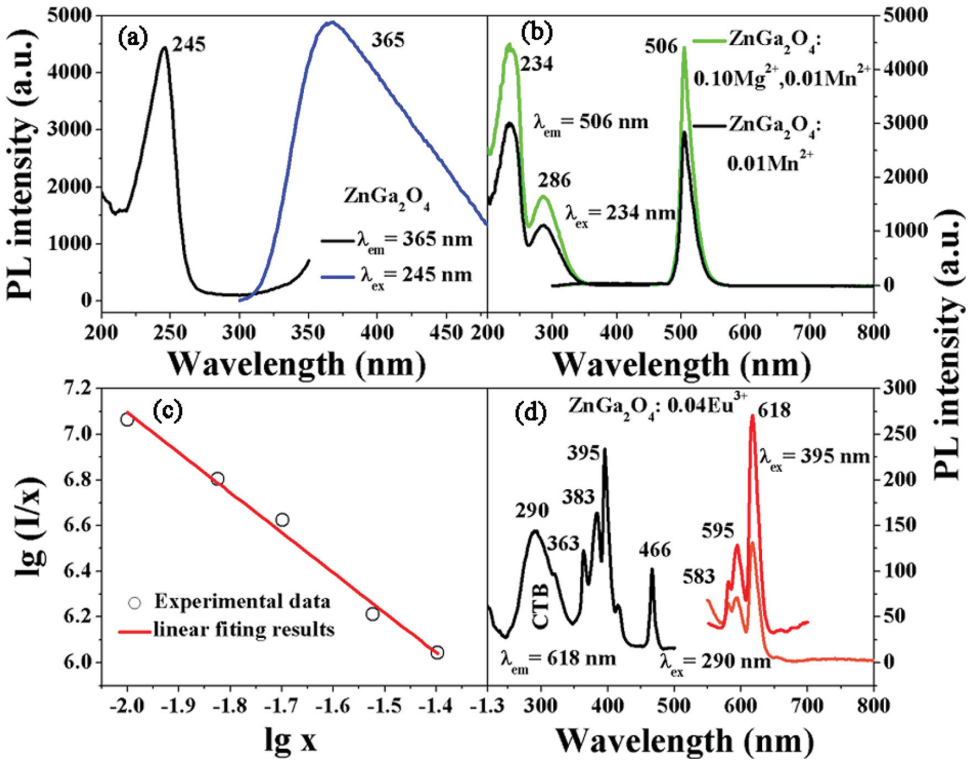

Figure 9. Photoluminescence excitation and emission spectra of a) $ZnGa_2O_4$-HT-1000 °C, b) $ZnGa_2O_4$: 0.01Mn^{2+}-HT-1000 °C, $ZnGa_2O_4$: 0.10Mg^{2+}, 0.01Mn^{2+}-HT-1000 °C. c) The relation of log (I/x) versus log (x) of Mn^{2+} ions. d) Photoluminescence excitation and emission spectra of $ZnGa_2O_4$: 0.04Eu^{3+}-HT-1000 °C.

calculated using the equation $R_C \approx 2\left[3V/4\pi X_C N\right]^{1/3}$ where V is the volume of the unit cell, N is the number of the host cations in the unit cell, and X_C is the critical concentration of doped ions.[30] For $ZnGa_2O_4$ host, $N = 8$ and $V = 579.01$ Å^3, X_C is 0.01 for Mn^{2+}, therefore, the critical distance (R_C) was calculated to be about 24.01 Å.

According to Dexter's theory, the concentration quenching is attributed to the interaction of multipolar-multipolar and the interaction intensity can be expressed by the PL intensity.[31]

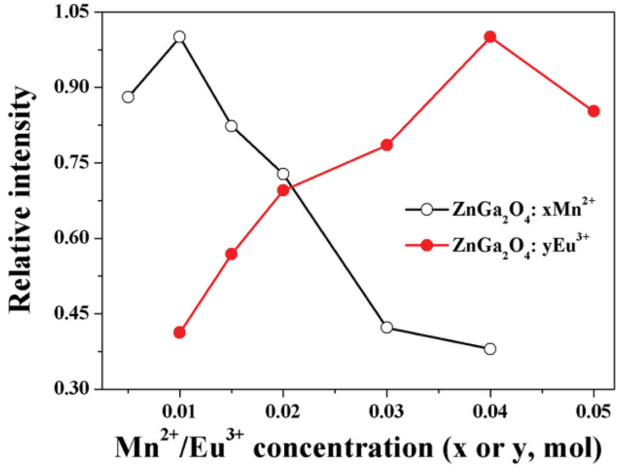

Figure 10. The PL intensity of Mn^{2+} (λ_{ex} = 234 nm) and Eu^{3+} (λ_{ex} = 395 nm) as a function of its doping concentration in $ZnGa_2O_4$ host.

The emission intensity I per activator of $ZnGa_2O_4$: Mn^{2+} phosphors can be expressed as

$$\frac{I}{x} = K\left[1+\beta(x)^{\theta/3}\right]^{-1}$$

where x is the concentration of activator, K and β are the constants for a given excitation wavelength and crystal structure.[32] The values of θ are 6, 8 and 10 mean dipole-dipole, dipole-quadrupole and quadrupole-quadrupole interaction, respectively. When x exceeds critical concentration, the equation can be simplified to

$$\frac{I}{x} = K'\left[\beta(x)^{\theta/3}\right]^{-1}$$

So the ratio of lg(I/x) and lg x presents the value of ($-\theta/3$).[7b] According to the above analysis, the value of θ in our experiment is approximately equal to 6 after calculating (Figure 9c), which indicates that the concentration quenching mechanism of $ZnGa_2O_4$: Mn^{2+} phosphors is dipole–dipole interaction.

The excitation and emission spectra of $ZnGa_2O_4$: 0.04Eu^{3+} phosphor are illustrated in Figure 9d. The excitation spectrum monitored with 618 nm consists of a broad band (maximum at 290 nm) and some narrow lines beyond 350 nm (maximum at 396 nm), which is due to the charge transfer band (CTB) of Eu^{3+}-O^{2-} together with absorption of $ZnGa_2O_4$ host lattice and the characteristic f–f transitions of Eu^{3+} within its $4f^6$

configuration.[12c] The charge transfer energy could be estimated by the equation $E_{CT} = [\chi(L) - \chi(M)](3\times10^4)$, where E_{CT} denotes the position of the CTB (in cm^{-1}) and $\chi(L)$ and $\chi(M)$ are the optical electronegativity of the anion and the central metal cation.[33] Taking $\chi(O) = 3.2$ and $\chi(Eu) = 1.75$, the band position for Eu^{3+}-O^{2-} CTB is calculated to be at 238 nm (about 42 000 cm^{-1}) which is lower than that of 290 nm obtained in the present $ZnGa_2O_4$: Eu^{3+} system, but the result is consistent with $BiPO_4$: Eu^{3+}, LaOF: Eu^{3+}, nanosized Y_2O_3: Eu^{3+}, YVO4: Eu^{3+} and sol-gel derived $ZnGa_2O_4$: Eu^{3+} systems.[12c,33a,34] The red shift of the CTB may result from the difference between bulk materials and nanoscale materials for the equation valued for bulk phosphors and the nephelauxetic effect.[33a,34c] In addition, the enhancement of the absorption intensity about the band from 350 to 400 nm comparing with the host material further confirms the absorption originating from Eu^{3+} ions, as shown in Figure S6 (Supporting Information). The excitation spectrum indicates that this material matches well with the commercial NUV LED chips (365–410 nm), thus, $ZnGa_2O_4$: Eu^{3+} may find potential application in WLEDs. Under the excitation of 395 nm irradiation, the emission spectrum is dominated by the hypersensitive red emission transition ($^5D_0$–$^7F_2$) accompanied by the presence of $^5D_0$–$^7F_1$ (583, 595 nm) transition, indicating that the Eu^{3+} ions are located at sites without inversion symmetry.[34b]

The photoluminescence decay curves of $ZnGa_2O_4$: $0.01Mn^{2+}$ and $ZnGa_2O_4$: $0.04Eu^{3+}$ samples were shown in **Figure 11**. Both of the decay curves of Mn^{2+} ($^4T_1$–$^6A_1$, 506 nm) and Eu^{3+} ($^5D_0$–$^7F_2$, 618 nm) could be well fitted to single exponential functions as $I = I_0 \exp(-t/\tau)$ (I_0 is the initial intensity at $t = 0$, τ is the $1/e$ lifetime), from which the life time of Mn^{2+} ($^4T_1$) and Eu^{3+} ($^5D_0$) were calculated to be 3.788 and 0.472 ms respectively, which are consistent with the previous reports.[7b,35]

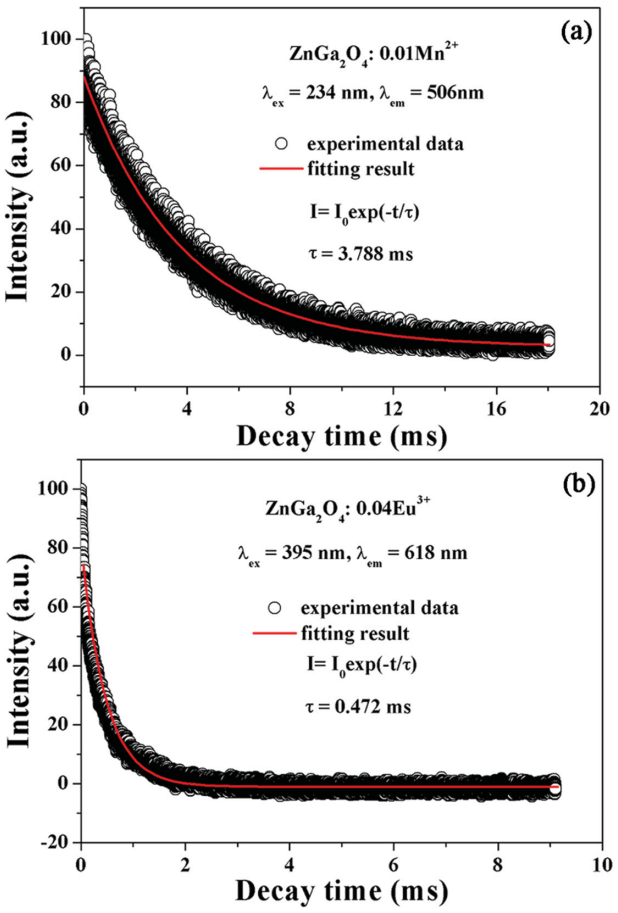

Figure 11. Photoluminescence decay curves for a) $ZnGa_2O_4$: $0.01Mn^{2+}$, λ_{em} = 506 nm; b) $ZnGa_2O_4$: $0.04Eu^{3+}$, λ_{em} = 618 nm. Black circles and red solid lines represent the experimental data and fitting results, respectively.

2.2.2. DFT Calculations

Considering a well-defined, periodic crystal structure, DFT calculations can be used to understand the electronic properties of the material and to explore the chemical bonding that occurs, which is beneficial for exploring superior luminescent materials and understanding the transitions about the photoluminescence process.[36] The calculated electronic band structure and density of states (DOS) of $ZnGa_2O_4$ are shown in **Figure 12**a,b. The result (Figure 12a) shows an electronic band gap of about 3.15 eV, which is smaller than the experimental result. This phenomenon is very common due to the insufficient description of the exchange correlation in DFT calculations, while this value is close to the previous DFT result of 3.10 eV.[14,36b,37] The highest occupied states and the lowest unoccupied states are mainly composed of O 2p and Zn 3d, to which the Ga 4s states make a small contribution due to the hybridization effect, as shown in Figure 12b. When a Mn atom replaces one of the Zn atoms, the Mn 3d majority spin states are fully occupied, and the main peak of the Mn 3d states appears at about the Fermi level (Figure 12c). It is clear that the valance band is dominant by the Mn 3d, while the Ga 4s and O 2p remain the dominant of the valance band. Thus, it is anticipated that Mn plays a critical role for the luminescence properties. Therefore, a separation of about 2.50 eV exists between the Mn 3d orbital and the bottom of valance band corresponding to the wavelength of 497 nm, which is very close to the experimentally observed emission wavelength of 506 nm in the $ZnGa_2O_4$: Mn^{2+} system. Similarly, an impurity band composed of Eu 4f states presents at about the Fermi level with width about 0.5 eV (Figure 12e), once introducing the Eu element. The energy separation of over 2.0 eV (wavelength about 622 nm) between the peaks of the Eu 4f orbitals and the bottom of valance band is consistent with the experimentally observed emission wavelength of 618 nm in the $ZnGa_2O_4$: Eu^{3+} system. Therefore, the $ZnGa_2O_4$ and $ZnGa_2O_4$: Mn^{2+}/Eu^{3+} are determined to emit blue light, green light and red light under UV illumination, respectively. Based on the above discussion, **Figure 13** presents a proposed mechanism of electron transition in the $ZnGa_2O_4$: Mn^{2+}/Eu^{3+} system. Initially, electronic transitions from the O 2p valence band to the Ga 4s conduction band occur under 200–400 nm UV radiation excitation. After excitation, the electron either relaxes to its ground state, producing a blue emission due to the self-activation center, or the excitation energy transfers to the mean peaks of Mn 3d and Eu 4f states near the lower band edge of conduction band. Then photoemission may occur, leading to the characteristic transition of Mn^{2+} ($^4T_1$–$^6A_1$) and Eu^{3+} ($^5D_0$–$^7F_{1,2}$).

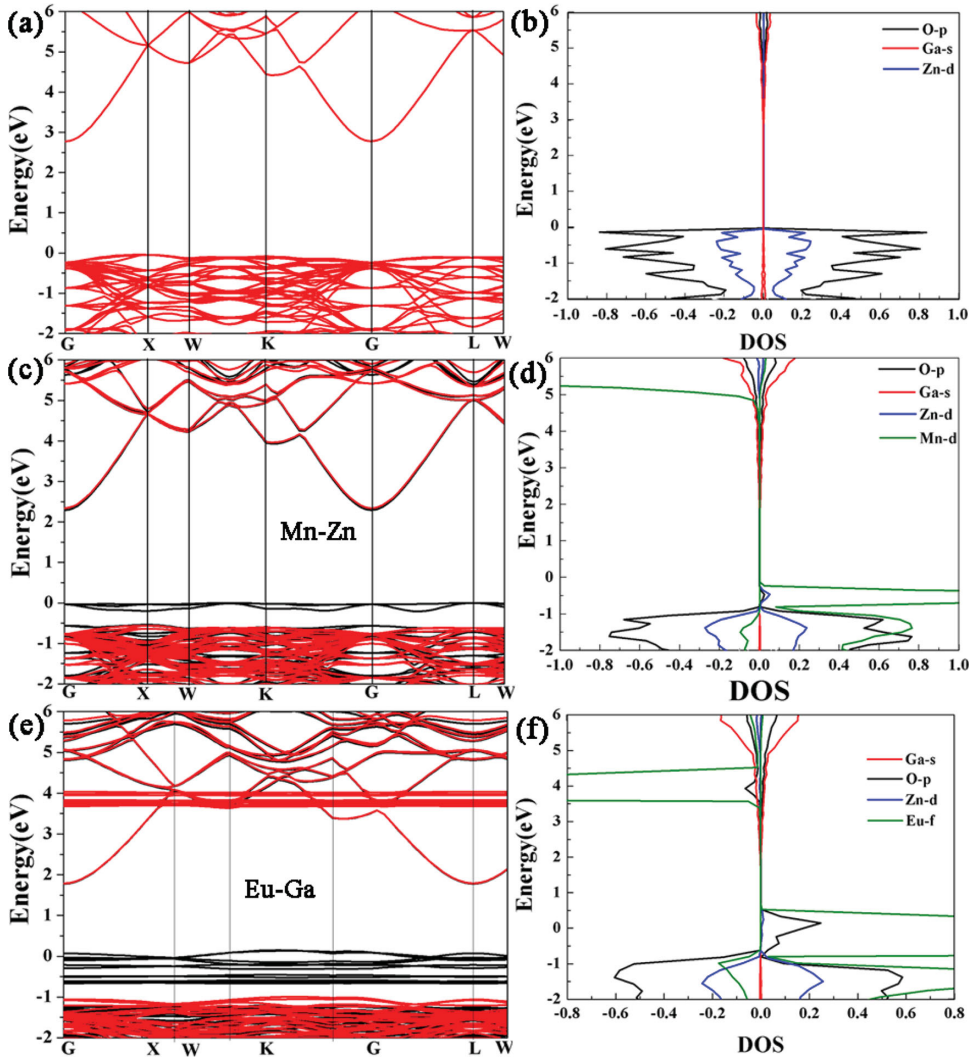

Figure 12. Band structures of a) pure $ZnGa_2O_4$, c) $ZnGa_2O_4$: $0.01Mn^{2+}$ and e) $ZnGa_2O_4$: $0.04Eu^{3+}$; The density of states (DOS) of b) pure $ZnGa_2O_4$, d) $ZnGa_2O_4$: $0.01Mn^{2+}$ and f) $ZnGa_2O_4$: $0.04Eu^{3+}$.

2.2.3. CL Properties

In order to explore the potential of the as-synthesized $ZnGa_2O_4$: Mn^{2+}/Eu^{3+} nanospheres used as luminescent materials in FEDs, their CL properties have been investigated in detail. Under the low-voltage electron-beam excitation, bright blue, green, and red luminescence emits from the undoped $ZnGa_2O_4$, $ZnGa_2O_4$: Mn^{2+}, and $ZnGa_2O_4$: Eu^{3+} nanospheres, respectively. The blue emission from the undoped $ZnGa_2O_4$ nanospheres is broad and peaked at 360 nm (**Figure 14**a), with the CIE chromaticity coordinates are $x = 0.226$ and $y = 0.252$ as shown in Figure 14d. It can be observed that the CL spectra of $ZnGa_2O_4$: $0.01Mn^{2+}$ samples show the emission at 506 nm under the excitation of 3 kV voltages, which corresponds to the characteristic emission of Mn^{2+} from $^4T_1$–$^6A_1$. The emission color is bright green to the naked eye with the CIE chromaticity coordinates (0.185, 0.541). For a purpose of comparison, the emission spectra of the $ZnGa_2O_4$: $0.01Mn^{2+}$ nanospheres (hydrothermal synthesized and annealed at different temperature), $ZnGa_2O_4$: $0.10Mg^{2+}$, $0.01Mn^{2+}$ (hydrothermal synthesized and annealed at 1000 °C for 3 h) and $ZnGa_2O_4$: $0.01Mn^{2+}$ bulk sample (prepared by solid state reaction annealed at 1200–1300 °C for 3 h) are also shown in Figure 14b. It can be seen that the CL intensity of $ZnGa_2O_4$: $0.01Mn^{2+}$-HT increases with the increase of the calcination temperature under the same conditions. The crystallinity of the samples would increase after annealing at 500 and 1000 °C, which can be confirmed by the XRD patterns shown in Figure 1. Thus, calcination is beneficial to enhance the CL intensity. On the other hand, the electrical resistance (sheet resistance R) of the samples decreases with the increasing of the calcination temperature as shown in **Figure 15**, which may be due to the increased crystallinity and the disappearance of organic additives during the calcination process confirmed by the TG-DSC curves shown in Figure S7 (Supporting Information). The higher electrical conductivity can help to dissipate the coulombic charge built up on the surface on the phosphors during the electron-beam bombardment, which will allow low-energy electrons reaching the phosphor grains,

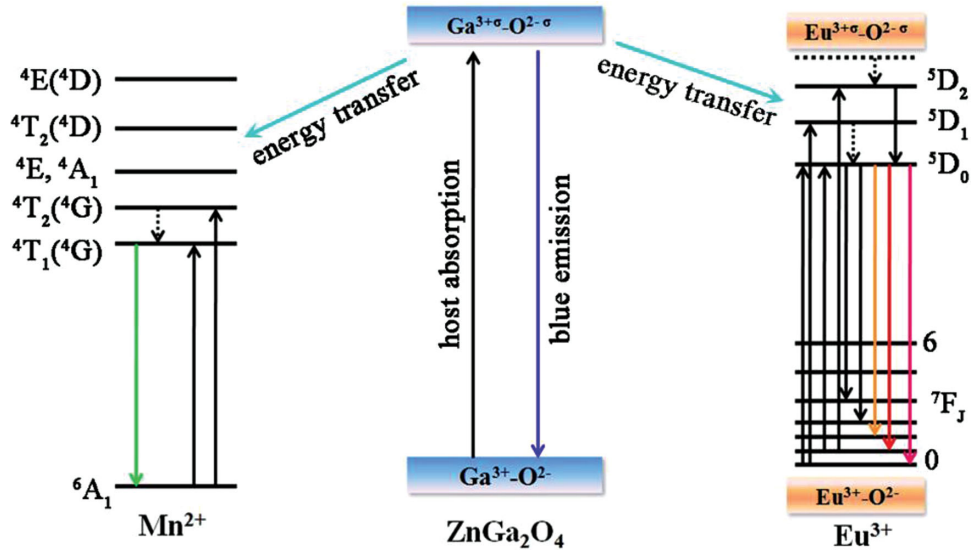

Figure 13. Possible mechanism of electronic transitions in $ZnGa_2O_4$ and $ZnGa_2O_4$: Mn^{2+}/Eu^{3+} system.

and thus increase the CL efficiency.[7c,38] In addition, it can be seen that the CL intensity of $ZnGa_2O_4$: 0.01Mn^{2+}-HT-1000 °C, $ZnGa_2O_4$: 0.10Mg^{2+}, 0.01Mn^{2+}- HT-1000 °C is higher than that of $ZnGa_2O_4$: 0.01Mn^{2+}-SSR-1200 °C, which proves that hydrothermal process not only reduce the synthesis temperature but also improve the luminescence intensity. This is due to the fact that the surface area of materials increases along with decrease in size, thus results in much more Mn^{2+} ions are excited under excitation.[39] In addition, the CL intensity has increased with the replacement of Mg^{2+} ions, which is consistent with the PL spectra. The red emission from the $ZnGa_2O_4$: 0.04Eu^{3+} nanospheres are peaked at 618 nm and can be assigned to the $^5D_0$–$^7F_2$ characteristic transition of Eu^{3+} ions as shown in Figure 14c, with the CIE chromaticity coordinates are x = 0.457 and y = 0.268. It is obvious that the straight line drawn between $ZnGa_2O_4$: Mn^{2+} (0.185, 0.541) and $ZnGa_2O_4$: Eu^{3+} (0.457, 0.268) would across the white zone, thus, tunable emission color would be obtained through changing the relative intensity of the two sources. In our system, we prepared a series of mixtures containing different ratios of $ZnGa_2O_4$: Mn^{2+} to $ZnGa_2O_4$: Eu^{3+} nanospheres. As shown in Figure 14e, the green emission gradually decreases and the red emission increases with the enhancement of the amount of $ZnGa_2O_4$: Eu^{3+}. As a result, a wide range of tunable color was obtained including white emission, as the photographs displayed inset of Figure 14e.

Furthermore, the CL emission intensities of $ZnGa_2O_4$, $ZnGa_2O_4$: 0.01Mn^{2+} and $ZnGa_2O_4$: 0.04Eu^{3+} have been investigated as a function of the accelerating voltage and the filament current, as shown in Figure S8. It is obvious that the emission intensities of all the samples increase with the enhancement of the accelerating voltages and filament currents without obvious saturation effect, respectively, which is attributed to the larger electron beam current density and deeper penetration depth.[40] The electron penetration depth can be estimated using the empirical formula $L[\text{Å}] = 250\ (A/\rho)(E/Z^{1/2})_n$, where $n = 1.2/(1–0.29 \log Z)$, A is the atomic or molecular weight of the material, ρ is the bulk density, Z is the atomic number or the number of electrons per molecule in the case of compounds, and E is the energy of the accelerating electron (keV).[3d] The enhancement of the electron penetration depth would produce more plasma, which could excite more activatots, and thus increase the CL emission intensity.[7a,7b,38,41] Because of their superior stability and strong CL intensity, these phosphors have potential applications in FEDs.

3. Conclusions

In summary, $ZnGa_2O_4$, $ZnGa_2O_4$: Mn^{2+} and $ZnGa_2O_4$: Eu^{3+} nanospheres were synthesized by a simple hydrothermal method with the assistance of Cit^{3-}, which respectively emit bright blue, green, and red luminescence under UV light and low-voltage electron beam irradiation. The electronic structure of the Mn 3d and Eu 4f are responsible for the green (Mn^{2+}) and red (Eu^{3+}) emission calculated from the DFT, respectively. The accomplishment of three primary colors (blue, green and red) indicates that $ZnGa_2O_4$ nanospheres hold great promise for full color display. Furthermore, the $ZnGa_2O_4$: Mn^{2+} nanospheres have a higher CL intensity than that of bulk due to more Mn^{2+} ions being excited. In addition, the PL and CL intensities of $ZnGa_2O_4$: Mn^{2+} nanospheres are increased because of the co-doping of Mg^{2+} ions. Due to their excellent CL intensity, good CIE chromaticity, superior stability and morphology uniformity, these phosphors have potential applications in lighting and display fields.

4. Experimental Section

Materials: The starting materials were commercial Ga_2O_3 (99.99%, Shanghai Sinopharm Chemical Reagent Co., Ltd.), Eu_2O_3 (99.999%, Science and Technology Parent Company of Changchun Institute of Applied Chemistry) and other chemicals were purchased from Beijing Chemical Company. All chemicals were analytical grade reagents and used directly without further purification.

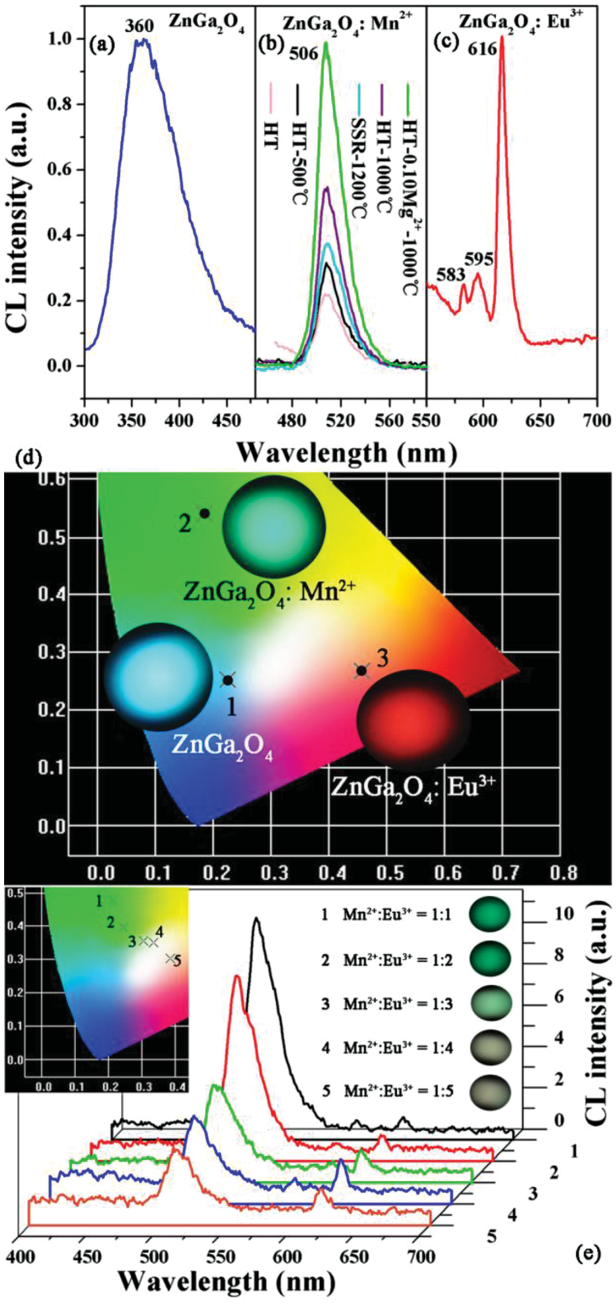

Figure 14. a) CL spectra of $ZnGa_2O_4$-HT-1000 °C; b) The comparison of CL spectra of $ZnGa_2O_4$: 0.01Mn^{2+}-HT-500/1000 °C, $ZnGa_2O_4$: 0.10Mg^{2+}, 0.01Mn^{2+}-HT-1000 °C and $ZnGa_2O_4$: 0.01Mn^{2+}-SSR-1200 °C; c) CL spectra of $ZnGa_2O_4$: 0.04Eu^{3+}-HT-1000 °C; d) The CIE chromaticity diagram for the $ZnGa_2O_4$, $ZnGa_2O_4$: 0.01Mn^{2+} and $ZnGa_2O_4$: 0.04Eu^{3+} samples under low voltage electron beam excitation, and the selected digital CL photographs (accelerating voltage = 3 kV, filament current = 90 mA). e) The CL spectra of mixtures containing different ratios of $ZnGa_2O_4$: Mn^{2+} to $ZnGa_2O_4$: Eu^{3+} nanospheres, and the corresponding photographs and CIE chromaticity coordinates.

Preparation: $GaCl_3$ (0.2 M) and $EuCl_3$ (0.1 M) stock solutions were obtained by dissolving the corresponding metal oxides in HCl solution at elevated temperature with agitation. Zn^{2+} (0.1 M) and Mn^{2+} (0.1 M) stock solutions were obtained by dissolving $Zn(CH_3COO)_2{\cdot}H_2O$ and $Mn(CH_3COO)_2{\cdot}4H_2O$ in deionized water with agitation. In a typical procedure, stoichiometry of Ga^{3+} and Zn^{2+} were added to 40 mL of deionized water. The mixture was stirred for 30 min. Then, certain quantity of trisodium citrate (Cit^{3-}) was added into the above solution (M:Cit^{3-} = 1:2 in moles, M = metal ions) and dilute HNO_3 was introduced rapidly into the vigorously stirred solution until pH = 5. After additional agitation for 20 min, the as-obtained solution was transferred to a 50 mL autoclave, sealed, and heated at 180 °C for 12 h, then cooled naturally to room temperature. The products were collected by centrifugation, washed three times with ethanol and deionized water. Finally, the products were dried at 80 °C for 12 h. The doped $ZnGa_2O_4$ samples were prepared by introducing proper amounts of Mn^{2+} and Eu^{3+} instead of Zn^{2+} and Ga^{3+} to the solution as described above. The Mg^{2+} ions codoped $ZnGa_2O_4$: Mn^{2+} samples were prepared by the same procedure above, except that a certain amount of $Mg(CH_3COO)_2 \cdot 4H_2O$ was used as the starting material. In addition, the stoichiometry amounts of ZnO, Ga_2O_3, and $MnCO_3$ were mixed in an agate mortar, adequately triturated and calcined in N_2/H_2 (95%/5%) at 1200–1300 °C for 3 h to synthesize $ZnGa_2O_4$: Mn^{2+} for comparison. To distinguish clearly, the products obtained by hydrothermal process and solid-state reaction were marked as $ZnGa_2O_4$: Mn^{2+}-HT and $ZnGa_2O_4$: Mn^{2+}-SSR, respectively.

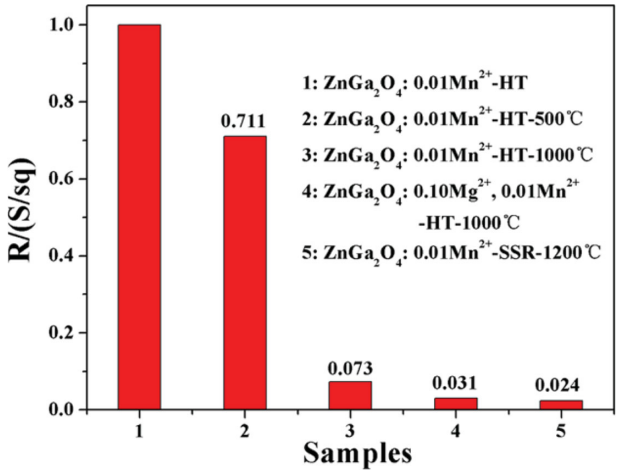

Figure 15. Variation of sheet resistance of $ZnGa_2O_4$: 0.01Mn^{2+}-HT-500/1000 °C, $ZnGa_2O_4$: 0.10Mg^{2+}, 0.01Mn^{2+}-1000 °C and $ZnGa_2O_4$: 0.01Mn^{2+}-SSR-1200 °C determined using a four-point probe.

Characterization: Power X-ray diffraction (XRD) measurements were performed on a D8 Focus diffractometer at a scanning rate of 10°/min in the 2θ range from 10° to 70°, with graphite monochromatized Cu Kα radiation (λ = 0.15405 nm). Raman spectrum was collected using a micro-Raman spectrometer (Renishaw) with a laser of 532 nm wavelength. XPS spectra were measured with a Thermo ESCALAB 250 instrument. Fourier transform infrared spectroscopy (FT-IR) was performed on a Perkin-Elmer 580B IR spectrophotometer using the KBr pellet technique. Diffuse reflectance spectra were taken on a Hatachi U-4100 UV–Vis–NIR spectrophotometer. Thermogravimetric and differential thermal analysis (TG-DTA) data were recorded with Thermal Analysis Instrument (SDT 2960, TA Instruments, New Castle, DE) with a heating rate of 10°/min in an air flow of 100 mL/min. The morphology and composition of the samples were inspected using a field-emission scanning electron microscope (FE-SEM, S-4800, Hitachi) equipped with an energy-dispersive X-ray (EDX) spectrometer. Transmission electronmicroscopy (TEM) were recorded using a FEI Tecnai G2S-Twin with a field-emission gun operating at 200 kV. Images were acquired digitally on a Gatan multipole CCD camera. PL excitation and emission spectra were recorded with a Hitachi F-7000 spectrophotometer equipped with a 150 W xenon lamp as the excitation source. CL measurements were carried out in an ultrahigh-vacuum chamber (<10–8 Torr), where the phosphors were excited by an electron beam in the voltage range of 2.0–6.0 kV and different filament currents, and the emission spectra were recorded using an F-7000 spectrophotometer. The

electrical conductivity of phosphor (sheet resistance R) was determined using a four-point probe. All the measurements were performed at room temperature (RT). Density functional theory (DFT) calculation for $ZnGa_2O_4$ was performed with the Vienna ab-initio simulation package (VASP). Details about the calculation are in the supporting information.

Supporting Information

Supporting Information is available from the Wiley Online Library or from the author.

Acknowledgements

This project is financially supported by the National Natural Science Foundation of China (NSFC 51332008, 51172227, 21221061), the Joint Funds of the National Natural Science Foundation of China and Guangdong Province (U1301242), and the National Basic Research Program of China (2010CB327704, 2014CB643803).

Received: June 24, 2014
Published online: August 26, 2014

[1] a) R. Yan, D. Gargas, P. Yang, *Nat. Photonics* **2009**, *3*, 569–576; b) Z. L. Wang, J. Song, *Science* **2006**, *312*, 242–246; c) M. R. Buck, R. E. Schaak, *Angew. Chem. Int. Ed.* **2013**, *52*, 6154–6178; d) C. Chen, C. Nan, D. Wang, Q. Su, H. Duan, X. Liu, L. Zhang, D. Chu, W. Song, Q. Peng, Y. Li, *Angew. Chem. Int. Ed.* **2011**, *50*, 3725–3729; e) U. Jeong, X. Teng, Y. Wang, H. Yang, Y. Xia, *Adv. Mater.* **2007**, *19*, 33–60; f) X. Huang, S. Han, W. Huang, X. Liu, *Chem. Soc. Rev.* **2013**, *42*, 173–201.

[2] a) M. Chen, C. Ye, S. Zhou, L. Wu, *Adv. Mater.* **2013**, *25*, 5343–5351; b) X. W. D. Lou, L. A. Archer, Z. Yang, *Adv. Mater.* **2008**, *20*, 3987–4019; c) M. Rycenga, C. M. Cobley, J. Zeng, W. Li, C. H. Moran, Q. Zhang, D. Qin, Y. Xia, *Chem. Rev.* **2011**, *111*, 3669–3712; d) H. G. Yang, C. H. Sun, S. Z. Qiao, J. Zou, G. Liu, S. C. Smith, H. M. Cheng, G. Q. Lu, *Nature* **2008**, *453*, 638–641.

[3] a) Q. Dai, M. E. Foley, C. J. Breshike, A. Lita, G. F. Strouse, *J. Am. Chem. Soc.* **2011**, *133*, 15475–15486; b) W.-T. Chen, H.-S. Sheu, R.-S. Liu, J. P. Attfield, *J. Am. Chem. Soc.* **2012**, *134*, 8022–8025; c) H. A. Höppe, *Angew. Chem. Int. Ed.* **2009**, *48*, 3572–3582; d) C. Liu, S. Zhang, Z. Liu, H. Liang, S. Sun, Y. Tao, *J. Mater. Chem. C* **2013**, *1*, 1305–1308; e) G. Li, Z. Hou, C. Peng, W. Wang, Z. Cheng, C. Li, H. Lian, J. Lin, *Adv. Funct. Mater.* **2010**, *20*, 3446–3456; f) R. J. Xie, N. Hirosaki, K. Sakuma, Y. Yamamoto, M. Mitomo, *Appl. Phys. Lett.* **2004**, *84*, 5404–5406; g) Q. Zhang, J. Wang, M. Zhang, W. Ding, Q. Su, *Appl. Phys. A.* **2007**, *88*, 805–809; h) L. Lin, X. Sun, Y. Jiang, Y. He, *Nanoscale.* **2013**, *5*, 12518–12531.

[4] S. Ye, F. Xiao, Y. X. Pan, Y. Y. Ma, Q. Y. Zhang, *Mater. Sci. Eng., R.* **2010**, *71*, 1–34.

[5] W.-R. Liu, C.-H. Huang, C.-W. Yeh, J.-C. Tsai, Y.-C. Chiu, Y.-T. Yeh, R.-S. Liu, *Inorg. Chem.* **2012**, *51*, 9636–9641.

[6] P. Psuja, D. Hreniak, W. Strek, *J. Nanomater.* **2007**, *2007*, 81350.

[7] a) G. S. R. Raju, J. Y. Park, H. C. Jung, E. Pavitra, B. K. Moon, J. H. Jeong, J. H. Kim, *J. Mater. Chem.* **2011**, *21*, 6136–6139; b) M. Shang, G. Li, D. Yang, X. Kang, C. Peng, Z. Cheng, J. Lin, *Dalton Trans.* **2011**, *40*, 9379–9387; c) J. Y. Kim, D. Y. Jeon, I. Yu, H. G. Yang, *J. Electrochem. Soc.* **2000**, *147*, 3559–3563.

[8] a) J. G. Li, X. Li, X. Sun, T. Ishigaki, *J. Phys. Chem. C.* **2008**, *112*, 11707–11716; b) G. Wakefield, E. Holland, P. J. Dobson, J. L. Hutchison, *Adv. Mater.* **2001**, *13*, 1557–1560.

[9] a) L. Wang, Z. Hou, Z. Quan, H. Lian, P. Yang, J. Lin, *Mater. Res. Bull.* **2009**, *44*, 1978–1983; b) L. Zou, X. Xiang, M. Wei, F. Li, D. G. Evans, *Inorg. Chem.* **2008**, *47*, 1361–1369; c) S. Y. Bae, J. Lee, H. Jung, J. Park, J.-P. Ahn, *J. Am. Chem. Soc.* **2005**, *127*, 10802–10803.

[10] Z. Gu, F. Liu, X. Li, J. Howe, J. Xu, Y. Zhao, Z. Pan, *J. Phys. Chem. Lett.* **2009**, *1*, 354–357.

[11] a) M. Allix, S. Chenu, E. Véron, T. Poumeyrol, E. A. Kouadri-Boudjelthia, S. Alahraché, F. Porcher, D. Massiot, F. Fayon, *Chem. Mater.* **2013**; b) W. Zhou, X. Yang, L. Huang, J. Wang, J. Tang, H. Liang, *Chem. Eur. J.* **2012**, *18*, 5367–5373.

[12] a) S. Y. Bae, H. W. Seo, C. W. Na, J. Park, *Chem. Commun.* **2004**, 1834–1835; b) L. Xu, Y. Su, Q. Zhou, S. Li, Y. Chen, Y. Feng, *Cryst. Growth Des.* **2007**, *7*, 810–814; c) M. Yu, J. Lin, Y. Zhou, S. Wang, *Mater. Lett.* **2002**, *56*, 1007–1013; d) Y. Li, X. Duan, H. Liao, Y. Qian, *Chem. Mater.* **1998**, *10*, 17–18.

[13] a) G. Kresse, J. Furthmüller, *Comp. Mater. Sci.* **1996**, *6*, 15–50; b) G. Kresse, J. Hafner, *Phys. Rev. B* **1993**, *47*, 558; c) G. Kresse, J. Furthmüller, *Phys. Rev. B* **1996**, *54*, 11169; d) J. P. Perdew, K. Burke, M. Ernzerhof, *Phys. Rev. Lett.* **1996**, *77*, 3865; e) K. Li, Y. Yan, H. Wang, Q. Zhan, Y. S. Mohammed, H. Jin, *Phys. Lett. A* **2010**, *374*, 628–631; f) N. Zu, J. Wang, Z. Wu, *J. Phys. Chem. C* **2013**, *117*, 7231–7235; g) H. J. Monkhorst, J. D. Pack, *Phys. Rev. B* **1976**, *13*, 5188–5192.

[14] H. Dixit, N. Tandon, S. Cottenier, R. Saniz, D. Lamoen, B. Partoens, V. Van Speybroeck, M. Waroquier, *New J. Phys.* **2011**, *13*, 063002.

[15] R. D. Shannon, *Acta Crystallogr. A* **1976**, *32*, 751–767.

[16] G. Van Gorkom, J. Haanstra, *J. Raman Spectrosc.* **1973**, *1*, 513–519.

[17] I. F. Li, C.-H. Su, H.-S. Sheu, H.-C. Chiu, Y.-W. Lo, W.-T. Lin, J.-H. Chen, C.-S. Yeh, *Adv. Funct. Mater.* **2008**, *18*, 766–776.

[18] C. Li, J. Yang, P. Yang, H. Lian, J. Lin, *Chem. Mater.* **2008**, *20*, 4317–4326.

[19] S. Huang, J. Xu, Z. Zhang, X. Zhang, L. Wang, S. Gai, F. He, N. Niu, M. Zhang, P. Yang, *J. Mater. Chem.* **2012**, *22*, 16136–16144.

[20] C. Li, J. Yang, Z. Quan, P. Yang, D. Kong, J. Lin, *Chem. Mater.* **2007**, *19*, 4933–4942.

[21] a) Y. Yin, A. P. Alivisatos, *Nature* **2004**, *437*, 664–670; b) H. C. Zeng, *J. Mater. Chem.* **2011**, *21*, 7511–7526.

[22] a) M. Ocana, R. Rodriguez-Clemente, C. J. Serna, *Adv. Mater.* **1995**, *7*, 212–216; b) Z. Xu, C. Li, Z. Hou, C. Peng, J. Lin, *CrystEngComm* **2011**, *13*, 474–482.

[23] C. Zhang, Z. Hou, R. Chai, Z. Cheng, Z. Xu, C. Li, L. Huang, J. Lin, *The J. Phys. Chem. C* **2010**, *114*, 6928–6936.

[24] Z. Fu, W. Xia, Q. Li, X. Cui, W. Li, *CrystEngComm* **2012**, *14*, 4618–4624.

[25] a) Y. Yang, O. Chen, A. Angerhofer, Y. C. Cao, *J. Am. Chem. Soc.* **2008**, *130*, 15649–15661; b) R. Buonsanti, D. J. Milliron, *Chem. Mater.* **2013**, *25*, 1305–1317; c) Y. Liu, D. Tu, H. Zhu, X. Chen, *Chem. Soc. Rev.* **2013**, *42*, 6924–6958.

[26] W. J. Yang, L. Y. Luo, T. M. Chen, N. S. Wang, *Chem. Mater.* **2005**, *17*, 3883–3888.

[27] a) Y. Zhang, G. Li, D. Geng, M. Shang, C. Peng, J. Lin, *Inorg. Chem.* **2012**, *51*, 11655–11664; b) C.-H. Huang, T.-M. Chen, *J. Phys. Chem. C* **2011**, *115*, 2349–2355.

[28] M. Osada, M. Takesada, T. Isobe, *ECS Trans.* **2009**, *16*, 75–80.

[29] L. Yu, H. Song, Z. Liu, L. Yang, S. L. Z. Zheng, *J. Phys. Chem. B* **2005**, *109*, 11450–11455.

[30] G. Blasse, *Philips Res. Rep.* **1969**, *24*, 131–144.

[31] D. L. Dexter, J. H. Schulman, *J. Chem. Phys.* **1954**, *22*, 1063–1070.

[32] L. Van Uitert, *J. Electrochem. Soc.* **1967**, *114*, 1048–1053.

[33] a) T. Grzyb, S. Lis, *Inorg. Chem.* **2011**, *50*, 8112–8120; b) Y. Su, L. Li, G. Li, *Chem. Mater.* **2008**, *20*, 6060–6067; c) P. Dorenbos, *J. Lumin.* **2005**, *111*, 89–104; d) P. Dorenbos, *J. Phys. Condens. Mater.* **2003**, *15*, 8417.

[34] a) M. Zhao, G. Li, L. Li, L. Yang, J. Zheng, *Cryst. Growth Des.* **2012**, *12*, 3983–3991; b) M. Yu, J. Lin, Z. Wang, J. Fu, S. Wang, H. Zhang, Y. Han, *Chem. Mater.* **2002**, *14*, 2224–2231; c) C. Shang, X. Shang, Y. Qu, M. Li, *Chem. Phys. Lett.* **2011**, *501*, 480–484.

[35] M. Shang, G. Li, X. Kang, D. Yang, D. Geng, C. Peng, Z. Cheng, H. Lian, J. Lin, *Dalton Trans.* **2012**, *41*, 5571–5580.

[36] a) C. C. Lin, Z. R. Xiao, G.-Y. Guo, T.-S. Chan, R.-S. Liu, *J. Am. Chem. Soc.* **2010**, *132*, 3020–3028; b) M. Mikami, *ECS J. Solid State Sci. Technol.* **2013**, *2*, R3048–R3058; c) F. Hintze, F. Hummel, P. J. Schmidt, D. Wiechert, W. Schnick, *Chem. Mater.* **2011**, *24*, 402–407; d) S. R. Römer, C. Braun, O. Oeckler, P. J. Schmidt, P. Kroll, W. Schnick, *Chem. Eur. J.* **2008**, *14*, 7892–7902.

[37] W. B. Park, K. H. Son, S. P. Singh, K.-S. Sohn, *ACS Comb. Sci.* **2012**, *14*, 537–544.

[38] C. Feldman, *Phys. Rev.* **1960**, *117*, 455–459.

[39] G. Li, C. Li, Z. Xu, Z. Cheng, J. Lin, *CrystEngComm* **2010**, *12*, 4208–4216.

[40] Q.-H. Zhang, J. Wang, C.-W. Yeh, W.-C. Ke, R.-S. Liu, J.-K. Tang, M.-B. Xie, H.-B. Liang, Q. Su, *Acta Mater.* **2010**, *58*, 6728–6735.

[41] X. Li, J. D. Budai, F. Liu, J. Y. Howe, J. Zhang, X.-J. Wang, Z. Gu, C. Sun, R. S. Meltzer, Z. Pan, *Light Sci. Appl.* **2013**, *2*, e50.